

Polymerized hybrid perovskites with enhanced stability, flexibility and lattice rigidity

Wenjing Chen

University of Science and Technology of China

Yongliang Shi

University of Science and Technology of China

Jia Chen

University of Science and Technology of China

Pingchuan Ma

University of Science and Technology of China

Zhibin Fang

University of Science and Technology of China

Dan Ye

University of Science and Technology of China

Yiyang Lu

University of Science and Technology of China

Yongbo Yuan

Central South University <https://orcid.org/0000-0002-4606-4611>

Jin Zhao

University of Science and Technology of China <https://orcid.org/0000-0003-1346-5280>

Zhengguo Xiao (✉ zhengguo@ustc.edu.cn)

University of Science and Technology of China <https://orcid.org/0000-0001-6646-1166>

Article

Keywords: organometal halide perovskites, soft lattice, lattice rigidity

Posted Date: January 19th, 2021

DOI: <https://doi.org/10.21203/rs.3.rs-129636/v1>

License: © ⓘ This work is licensed under a Creative Commons Attribution 4.0 International License.

[Read Full License](#)

Version of Record: A version of this preprint was published at Advanced Materials on September 30th, 2021. See the published version at <https://doi.org/10.1002/adma.202104842>.

1 **Polymerized hybrid perovskites with enhanced stability, flexibility and lattice rigidity**

2 Wenjing Chen^{1†}, Yongliang Shi^{1†}, Jia Chen¹, Pingchuan Ma¹, Zhibin Fang¹, Dan Ye¹, Yiyang
3 Lu¹, Yongbo Yuan², Jin Zhao¹, Zhengguo Xiao^{1*}

4 ¹Hefei National Laboratory for Physical Sciences at the Microscale, CAS Key Laboratory of
5 Strongly-coupled Quantum Matter Physics, Department of Physics, University of Science and
6 Technology of China, Hefei, Anhui 230026, China

7 ²Hunan Key Laboratory of Supermicrostructure and Ultrafast Process, School of Physics and
8 Electronics, Central South University, Changsha, Hunan 410083, China

9 [†]These authors contribute equally to this work

10 *Correspond to: zhengguo@ustc.edu.cn

11
12 **Abstract: The intrinsic soft lattice nature of organometal halide perovskites (OHPs)**
13 **makes them very tolerant to defects and ideal candidates for solution-processed**
14 **optoelectronic devices. However, the soft lattice results in low stability towards external**
15 **stresses such as heating and humidity, and induces high density of phonons, causing**
16 **strong electron-phonon coupling. Here, we report solid-state polymerization of OHPs**
17 **using unsaturated 4-vinylbenzylammonium as organoammonium cations without**
18 **damaging perovskite structure and its tolerance to defects. The polymerized perovskites**
19 **show enhanced stability and flexibility compared to regular three-dimensional and two-**
20 **dimensional perovskites. Furthermore, the polymerized 4-vinylbenzylammonium group**
21 **improves perovskite lattice rigidity substantially, resulting in reduced electron-phonon**
22 **coupling and non-radiative recombination rate, and enhanced carrier mobility because**
23 **of suppressed phonon scattering. We demonstrate efficient polymerized perovskite based**
24 **light-emitting diodes with an external quantum efficiency of 23.2% and enhanced**
25 **operation stability.**

26 **Introduction**

27 Organometal halide perovskites (OHPs), including three-dimensional (3D) and two-
28 dimensional (2D) perovskite (Ruddlesden-Popper (RP) and Dion-Jacobson (DJ) phases), have
29 become as a new generation of semiconducting materials for electronic and optoelectronic
30 devices¹⁻⁴. An intrinsic nature of OHPs is its soft lattice due to weak ionic bonding between
31 metal and halide, and non-covalent bonding between organic cations and the inorganic
32 framework⁵. The soft lattice nature makes OHPs very tolerant to defects compared to
33 conventional inorganic semiconductors such as silicon and III-V compounds⁶⁻⁸, making OHPs
34 ideal candidates for solution-processed optoelectronic devices. However, the soft lattice results
35 in low stability towards external stresses such as heating and humidity^{7,9}. In addition, it induces
36 high density of phonons, causing strong electron-phonon coupling (EPC) in OHPs^{10,11},
37 particularly in 2D RP phase with weak Van der Waals force between adjacent organic layers¹²⁻
38 ¹⁴. The strong EPC results in rapid non-radiative exciton quenching, and low
39 photoluminescence quantum yield (PLQY)¹⁴⁻¹⁶, which is detrimental to devices working at
40 high temperature or under high current density. For example, perovskite light-emitting diodes
41 (PeLEDs) based on 2D OHPs, such as phenethylammonium lead iodide, has
42 electroluminescence only at liquid nitrogen temperature¹⁷.

43 There are many small ligands and polymer ligands explored to improve the stability and/or
44 optoelectronic properties of OHPs, such as those containing C=O group¹⁸⁻²¹ and hydrophobic
45 group²². Their functions include trap passivation^{19,20}, making the film more hydrophobic^{21,22},
46 improving the film quality^{21,23}, and/or suppression of ion migration¹⁸, etc. (Supplementary
47 Table 1). In general, the polymer ligands work as additives located at the grain boundary

48 (Supplementary Fig. 1), and form polymer-perovskite mixture, rather than in the perovskite
49 lattice¹⁸⁻²². A limitation of those approaches is that the polymer additives cannot change the
50 intrinsic properties of OHPs such as their strong EPC, although they can form coordinate
51 bonding with the metallic lead or dangling bonds of halides at the crystal surface.

52 In this work, we report solid-state polymerization (SSP) of perovskite lattice using
53 unsaturated organoammonium cations 4-vinylbenzylammonium (VBA) without damaging the
54 perovskite structure. The polymerized perovskite, a new phase of OHPs which is different from
55 RP or DJ phase, shows polymer-like behavior such as enhanced water/thermal stability and
56 flexibility, resulted from the high molecular weight of the polymerized-VBA (PVBA) ligands
57 and strong covalent C-C bonding between adjacent organoammonium groups. More excitingly,
58 as organic component of the perovskite structure which is superior to regular polymer additives,
59 the PVBA ligands increase rigidity of perovskite lattice without scarifying its tolerance to
60 defects, resulting in less activated optical phonon modes and weakened EPC, suppressed non-
61 radiative exciton recombination rate, as well as increased electron/hole mobility due to less
62 phonon scattering. Benefitted from the above advantages of polymerized perovskite, high-
63 performance PeLEDs with a record external quantum efficiency (EQE) of 23.2 % and improved
64 operation stability was achieved.

65 **Theoretical prediction of the formation of polymerized perovskite.**

66 SSP within the organic component of the perovskite structure depends highly on the molecular
67 structure of organoammonium ligands^{24,25}. Firstly, the distance between two adjacent C=C
68 functional groups in the perovskite lattice before polymerization should be less than 5 Å to
69 activate SSP²⁵. Secondly, the distance between two adjacent ammonium ligands (d_{N-N}) after

70 polymerization should match the distance between two adjacent metal-halide octahedral (d_{M-M})
71 M). Lastly, ammonium ligands should be susceptible to polymerization without additional
72 initiators. VBA has a similar structure with phenylmethylammonium (PMA), a very popular
73 ligand in 2D perovskites, but has an unsaturated vinyl group in para position of the aromatic
74 phenyl ring (Fig. 1a). The styrene group in VBA monomer enables easy polymerization under
75 UV irradiation or low-temperature heating^{26,27}. Therefore, we select VBA monomer as the
76 organoammoniums for SSP. As shown in Fig. 1a, the styrene groups are first excited to a singlet
77 state by UV irradiation or heating²⁷, followed by intersystem crossing to a triplet state and
78 formation of radicals on the vinyl carbons. The radicals then form new covalent bonds with
79 other nearby vinyl groups²⁶, forming PVBA ligands.

80 We first estimated the feasibility of forming polymerized perovskite phase with VBA
81 monomer and their molecular configuration before and after SSP using density functional
82 theory (DFT) (see Methods). Fig. 1b and Supplementary Fig. 2a show the calculated molecule
83 structure of $(VBA)_2PbI_4$ perovskite with VBA before polymerization, which is similar with that
84 of $(PMA)_2PbI_4$ ²⁸. The distances between adjacent unsaturated C=C bonds are 3.8 and 4.1 Å
85 (Fig. 1c), satisfying the criteria for the SSP. Our calculation shows that the Gibbs free energy
86 of $(VBA)_2PbI_4$ decreases by 3.6 eV per unit after SSP, indicating easy formation and
87 stabilization of polymerized- $(VBA)_2PbI_4$ (noted as $(PVBA)_2PbI_4$). Fig. 1d and Supplementary
88 Fig. 2b show a molecular structure of $(PVBA)_2PbI_4$, which has the lowest Gibbs free energy.
89 The d_{N-N} in the $(PVBA)_2PbI_4$ structure varies from 5.3 to 7.7 Å depending on tilting angle of
90 the aromatic phenyl ring (Fig. 1e), matching d_{M-M} of methylammonium lead
91 iodide/bromide/chloride (6.3 Å, 5.9 Å, 5.7 Å, respectively)²⁹.

92 It should be noted that the SSP process causes minor structural changes in the perovskite
93 lattice, as predicted by DFT calculation. For example, the distance between two inorganic
94 layers reduces from 18.3 Å to 17.2 Å due to formation of strong covalent bonding between two
95 adjacent VBA layers (Fig. 1b,d). The orientations of phenyl rings in adjacent VBA layers
96 change from vertical to parallel after SSP, in order to minimize their repulsion interaction. The
97 average Pb-I-Pb angles also slightly increase from 148.1° to 152.7° to adapt to the configuration
98 of PVBA (Fig. 1f). As a result of the greater Pb s and I p orbital overlap, the bandgap of
99 (VBA)₂PbI₄ is reduced by 0.06 eV after SSP (Supplementary Fig. 2). Nevertheless, regardless
100 of those above minor configuration changes, the (VBA)₂PbI₄ retain its perovskite structure
101 after SSP.

102 **Experimental evidences demonstrating the formation of polymerized perovskite.**

103 We first synthesized VBAI monomer (see Methods), and then mixed it with PbI₂ in
104 dimethylformamide (DMF) to prepare perovskite films. Interestingly, the mixed VBAI-PbI₂
105 (2:1 molar ratio) solution (1 M) changes from liquid before polymerization to viscous colloidal
106 after polymerization under UV irradiation (Supplementary Fig. 3), suggesting polymerization
107 of VBA monomers in the solution. Perovskite-like absorption, PL, and X-ray diffraction (XRD)
108 patterns of the films (Fig. 2a,b), similar to 2D (PMA)₂PbI₄ perovskite (Supplementary Fig. 4),
109 suggest that 2D (VBA)₂PbI₄ perovskite with VBA monomer in the lattice is formed. As
110 expected, the 2D (VBA)₂PbI₄ film maintain its perovskite structure after polymerization under
111 UV irradiation, evidenced from its sustained perovskite-like characteristics. Interestingly, the
112 minor structural and bandgap changes after SSP, as predicted by DFT calculation, were also
113 experimentally observed. As shown in Fig. 2a,b, both absorption edge and PL peak slightly

114 redshifts, and d-spacing of (002) plane ($d_{(002)}$) gradually decreases from 18.1 Å to 17.2 Å.

115 Fourier transform infrared spectroscopy (FTIR), proton nuclear magnetic resonance (^1H
116 NMR) were used to track the polymerization process of VBA monomers in the 2D $(\text{VBA})_2\text{PbI}_4$
117 perovskite structure. As shown in Fig. 2c, the C=C stretching, and =CH₂ and =CH wagging
118 vibration peaks from vinyl group gradually disappear with UV exposure time increasing from
119 10 to 60 min, indicating the polymerization of VBA monomers in the $(\text{VBA})_2\text{PbI}_4$ films. The
120 ^1H NMR peaks assigned to the vinyl group decrease obviously with the appearance of new
121 peaks in the sp^3 carbon region at 2.5 ppm, resulted from polymerization of vinyl group (Fig.
122 2d). In addition, the peaks come from aromatic proton are partially shifted to around 7.0 ppm
123 due to the shielding effect caused by polymerization. By normalizing the known quantity of
124 tetramethylsilane (TMS, as the internal standard material), the percentage of polymerized VBA
125 monomers can be calculated by comparing the integral area of a, b, and c peaks before and
126 after polymerization. It is shown that around 65% of VBA monomers are polymerized after
127 UV for 60 min. Gel permeation chromatography (GPC) was conducted to investigate the degree
128 of polymerization (DP) of VBA monomers in $(\text{PVBA})_2\text{PbI}_4$ films. As shown in Fig. 2e, the
129 average molecular weight (M_n) of PVBA is positively correlated with the UV exposure time
130 with DP ranging from 4 to 75.

131 In addition to $(\text{PVBA})_2\text{PbI}_4$ perovskite, a series of quasi-2D perovskite films with different
132 dimensions $(\text{PVBA})_2\text{MA}_{n-1}\text{Pb}_n\text{I}_{3n+1}$ were also successfully prepared. They all show
133 characteristics of quasi-2D perovskites in absorption, PL, as well as XRD (Supplementary Fig.
134 5). The d-spacing of $(\text{PVBA})_2\text{MA}_{n-1}\text{Pb}_n\text{I}_{3n+1}$ films calculated from (001) peak of XRD match
135 well with the high-resolution transmission electron microscopy (HRTEM) images and DFT

136 calculations (Supplementary Fig. 6), demonstrating the formation of $(\text{PVBA})_2\text{MA}_{n-1}\text{Pb}_n\text{I}_{3n+1}$
137 perovskite structure.

138 **The polymerized perovskite with enhanced stability.**

139 A very attractive property of polymerized perovskite is its enhanced intrinsic stability.
140 Thermogravimetric analysis (TGA) was used to investigate the thermal stability of the
141 $(\text{PVBA})_2\text{PbI}_4$ film. As shown in Fig. 2f, three stages of TGA curves are observed, which can
142 be attributed to loss of VBA capping layer at the surface, organic amine salt in the perovskite
143 framework, and PbI_2 , respectively³⁰. An obvious delay is observed in the organic species of
144 $(\text{VBA})_2\text{PbI}_4$ after UV treatment, suggesting better thermal stability after polymerization. The
145 improved thermal stability can be attributed to the strong covalent bond between
146 organoammonium ligands between adjacent layers, and higher molecular weight of PVBA than
147 VBA monomer.

148 The polymerized perovskite $(\text{PVBA})_2\text{PbI}_4$ also has much improved humid stability. We
149 directly soaked both $(\text{VBA})_2\text{PbI}_4$ and $(\text{PVBA})_2\text{PbI}_4$ films in water without any encapsulation
150 (Supplementary Video 1). Fig. 2g shows the photographs of the films immersed in water for
151 different time. The control film degrades rapidly in seconds, while the polymerized perovskite
152 $(\text{PVBA})_2\text{PbI}_4$ film remain unchanged for 30 s. In addition to the above reasons for enhanced
153 thermal stability, the improved humid stability may also benefit from the increased
154 hydrophobicity of PVBA.

155 Benefited from its polymer-like behavior, the polymerized perovskite shows greatly
156 enhanced flexibility. Fig. 2h shows scanning electron microscopy (SEM) images of the
157 $(\text{VBA})_2\text{PbI}_4$ and $(\text{PVBA})_2\text{PbI}_4$ films (thickness 500 nm) upon 500 bending cycles with a

158 bending radius of 3 mm. The $(\text{VBA})_2\text{PbI}_4$ film shows many cracks while the polymerized
159 perovskite $(\text{PVBA})_2\text{PbI}_4$ remains very compact, demonstrating its potential in flexible devices.

160 **The polymerized perovskite with enhanced lattice rigidity.**

161 Another exciting property of polymerized perovskite is its enhanced lattice rigidity because of
162 the polymerized carbon chains in the lattice. This is in direct contrast with the polymer-
163 perovskite mixture film with polymers at the grain boundary^{18,21}. We first calculated average
164 atomic displacement of $(\text{PVBA})_2\text{PbI}_4$, and $(\text{PMA})_2\text{PbI}_4$ as control, at different temperatures
165 using DFT (see Methods). As shown in Fig. 3a, the root mean squared displacement (RMSD)
166 of carbon atoms in $(\text{PVBA})_2\text{PbI}_4$ is a half of that of control $(\text{PMA})_2\text{PbI}_4$ structure due to the
167 restricted motions of carbon atoms after polymerization. Notably, resulted from the interaction
168 between organic and inorganic components in the perovskite structure, the RMSD of both Pb
169 and I atoms are also smaller in $(\text{PVBA})_2\text{PbI}_4$ as temperature increasing from 80 K to 380 K.
170 Fig. 3b shows the DFT calculated real-space displacement of both $(\text{PVBA})_2\text{PbI}_4$ and
171 $(\text{PMA})_2\text{PbI}_4$ structures. It is clear that the displacement of I atom, whose orbitals form the
172 valence band maximum (VBM) and conduction band minimum (CBM), is suppressed in
173 $(\text{PVBA})_2\text{PbI}_4$. The displacement of heavy Pb atoms is much smaller than the I atoms. The atom
174 displacement cause fluctuations in the electronic bandstructure. Obviously, the time variation
175 of both VBM and CBM in $(\text{PVBA})_2\text{PbI}_4$ are smaller than that of $(\text{PMA})_2\text{PbI}_4$ structure (Fig.
176 3c).

177 The higher rigidity results in less activated optical phonon modes and weaker EPC in
178 $(\text{PVBA})_2\text{PbI}_4$ perovskite¹⁴. Temperature-dependent steady-state PL was conducted to
179 investigate the strength of EPC in the perovskite films (Supplementary Fig. 7). It has been

180 demonstrated that EPC dominates the line broadening in various 2D perovskite, and the
181 contribution from impurities can be neglected³¹. As shown in Fig. 3d,e, the (PVBA)₂PbI₄ film
182 has obviously smaller full-width at half-maximum (FWHM) than the control (PMA)₂PbI₄ film,
183 particularly at high temperature.. The deformation potential (*D*) defined as the shift in energy
184 band per unit strain¹⁴, which can be used to quantify the EPC strength, is reduced from 1.3×10⁹
185 eV/cm in (PMA)₂PbI₄ to 8.7×10⁸ eV/cm in (PVBA)₂PbI₄ (see Methods).

186 Weak EPC is expected to reduce non-radiative recombination rates of excitons in
187 perovskite³². Both temperature-dependent PLQY and carrier lifetime (*T_{average}*) were measured
188 to examine the recombination dynamics of the polymerized perovskite (Supplementary Fig. 7).
189 Radiative and non-radiative recombination rate (*k_{rad}* and *k_{non}*, respectively) are calculated using
190 equations $\frac{1}{T_{average}} = k_{rad} + k_{non}$ and $PLQY = \frac{k_{rad}}{k_{rad} + k_{non}}$. As shown in Fig. 3f,g, the *k_{non}* of
191 (PMA)₂PbI₄ increase dramatically with temperature up to 380 K, in contrast to the slight
192 increase of (PVBA)₂PbI₄ films. Considering that the trap densities of (PVBA)₂PbI₄ and
193 (PMA)₂PbI₄ calculated by space-charge limited current (SCLC) measurement are similar
194 (Supplementary Fig. 8), the dramatic difference in the *k_{non}* of (PVBA)₂PbI₄ and (PMA)₂PbI₄ is
195 therefore result from the EPC difference (Fig. 3f,g).

196 In addition to charge recombination dynamics, EPC also influence charge transportation
197 due to phonon scattering^{33,34}. Temperature-dependent SCLC was measured to examine the
198 influence of EPC on carrier mobility (Supplementary Fig. 9). As shown in Fig. 3h,i, two
199 regimes are identified corresponding to orthorhombic and tetragonal phases. Both regimes can
200 be fitted by a power law, $\mu \propto T^{-m}$, where *m* is a co-efficient indicating strength of EPC³⁵. In

201 both regimes, the exponent (m) of $(PVBA)_2PbI_4$ are smaller than that of $(PMA)_2PbI_4$ for both
202 electron and hole mobility, indicating that weaker EPC in the polymerized perovskite.

203 **The polymerized PeLEDs.**

204 As an application of polymerized perovskite, we fabricated PeLEDs using $(PVBA)_2MA_{n-1}Pb_nI_{3n+1}$
205 films with a structure of ITO/poly-TPD/perovskite/TPBi/LiF/Al (ITO: indium tin
206 oxide, poly-TPD: poly[N,N'-bis (4-butylphenyl)-N,N'-bis(phenyl)-benzidine], TPBi: 2,2',2''-
207 (1,3,5-Benzinetriyl)-tris(1- phenyl-1-H-benzimidazole)). It should be noted that the quasi-2D
208 perovskite films consist several phases with different n values. Fig. 4a shows energy level
209 diagram of the devices, and the carriers transfer from large bandgap perovskite (small n phases)
210 to small bandgap ones (large n phases)^{36,37}. The strong EPC in small n phases causes non-
211 radiative recombination and thus charge loss during the energy transfer process (Fig. 4a). The
212 polymerized perovskite with weak EPC suppresses this loss and results in higher PLQY. For
213 example, the PLQY increases from 32.8% for control $(PMA)_2(MA)_9Pb_{10}I_{31}$ film to 45.7% for
214 $(PVBA)_2(MA)_9Pb_{10}I_{31}$ film, which should be attributed to their different EPC as both films
215 have similar trap density (Supplementary Fig. 8). The EQE of the PeLEDs increase from 12.5%
216 to a decent value of 17.6% accordingly (Fig. 4b). The EQEs of polymerized perovskite
217 $(PVBA)_2MA_{n-1}Pb_nI_{3n+1}$ ($n=2, 5, 7, 10, 20$) based PeLEDs are much higher than that of control
218 PeLEDs, particularly for devices with small $\langle n \rangle$ films ($\langle n \rangle$ is the value for stoichiometric
219 quasi-2D perovskite in solution) (Fig. 4c). The EQE is further improved to a record value of
220 23.2%, approaching to the out-coupling limit of 24.7% (Supplementary Fig. 10), using popular
221 mixed-cations and mixed-halides perovskite $(PVBA)_2(FA_{0.83}Cs_{0.17})_9Pb_{10}(I_{0.9}Br_{0.1})_{31}$ (FA:
222 formamidinium). The higher EQE should be due to their better film crystallinity of mixed-

223 cation perovskites³⁸, evidenced by its higher external PLQY value of 56.8%. The internal
224 quantum yield reaches 93.5% assuming both charge carrier balance and radiative excitons are
225 unity. This value is slightly different with that calculated from the PLQY values (91.2%, as the
226 escape probability of photon is 12.7%³⁹) due to their different carrier concentrations. The
227 current density-voltage (J - V), angular spectra and intensity profiles, and EQE curves of the
228 devices are shown in Supplementary Fig. 11-12. Notably, the electroluminescence (EL) spectra
229 of polymerized perovskite based PeLEDs are generally sharper than that of (PVBA)₂MA_{n-}
230 ₁Pb_nI_{3n+1} PeLEDs (Fig. 4d), further demonstrating weaker EPC in the emissive low-bandgap
231 domains in the PeLEDs.

232 We conducted temperature-dependent measurement to examine the effect of EPC on
233 device performance using $n=2$ perovskites as examples because there are more small n
234 phases in the films (Supplementary Fig. 13). As shown in Fig. 4e, the EQE of the control
235 PeLEDs decrease dramatically with temperature compared to that of (PVBA)₂MAPb₂I₇ based
236 PeLEDs. This result demonstrates that the EPC plays a critical role in PeLEDs.

237 We finally measured the operation stability (T_{50} , time to half of the initial luminance) under
238 a constant current density of 5 mA/cm² in a N₂ glove-box without encapsulation. The T_{50} of
239 (PVBA)₂MAPb₂I₇ based PeLEDs reached 20.8 h, much longer than the control PeLEDs (Fig.
240 4f). The better operation stability can be ascribed to the more stable structure of polymerized
241 perovskite than (PMA)₂MAPb₂I₇.

242 **Discussion**

243 We have demonstrated the formation of polymerized perovskite using unsaturated
244 organoammonium ligands. The polymerized perovskites show polymer-like behavior such as

245 improved film stability and flexibility, in contrast to regular RP and DJ phases with ammonium
246 functional monomers. Compared to various polymer additives reported previously
247 (Supplementary Table 1), a unique advantage for polymerized perovskite is that PVBA ligands
248 are in the perovskite lattice and forms perovskite structure with metal-halide octahedron.
249 Benefitted from the polymerized perovskite structure, the strong C-C covalent bond in PVBA
250 can reduce ion vibration of metal-halide octahedron and increase lattice rigidity. The increased
251 lattice rigidity further suppresses EPC of OHPs, leading to suppressed nonradiative
252 recombination rate, small PL/EL FWHM, as well as increased carrier mobility without
253 sacrificing its tolerance to defects. PeLEDs made from $(PVBA)_2(FA_{0.83}Cs_{0.17})_9Pb_{10}I_{31}$ showed
254 a decent EQE of 23.2% with improved operation stability. Our discovery of polymer perovskite
255 opens up a new way to design perovskites to improve their intrinsic stability, and tune the
256 physical property of perovskites.

257 **Methods**

258 *Materials.* Chemicals used in the experiments include lead iodide (PbI_2 ; 99.999%, Alfa-Aesar),
259 cesium iodide (CsI ; 99.999%, Alfa-Aesar), formamidinium iodide (FAI; 99%, Xi'an Polymer
260 Light Technology Corp), lead bromide ($PbBr_2$; 99.999%, Alfa-Aesar), poly[N,N'-bis (4-
261 butylphenyl)-N,N'-bis(phenyl)-benzidine] (poly-TPD; American Dye Source Inc.), 2,2',2''-
262 (1,3,5-Benzinetriyl)-tris(1-phenyl-1-H-benzimidazole) (TPBi; Lumtech Inc.), lithium fluoride
263 (LiF ; 98.5%; Alfa-Aesar), N,N-dimethylformamide (DMF; 99.8%, Sigma-Aldrich),
264 chlorobenzene (CB; 99.8%, Sigma-Aldrich), toluene (99.8%, Sigma-Aldrich).

265 Methylammonium iodide (MAI) (or phenylmethylammonium iodide, PMAI) was
266 synthesized by mixing methylamine (40 wt.% in H_2O , Sigma-Aldrich) (or phenylmethylamine,

267 99%, Sigma-Aldrich) with equimolar amounts of aqueous hydriodic acid (HI; 57 wt.% in H₂O,
268 Sigma-Aldrich) at 0 °C with constant stirring for 2 h. The solvent was then evaporated under
269 reduced pressure at 65 °C. The remaining white solid product were purified by recrystallization
270 in ethanol, and the recrystallized solid were dried in the N₂ glove-box at 60 °C for 24 h. VBAI
271 was synthesized using a similar procedure with PMAI. 4-vinylbenzylamine (92%, stabilized
272 with 4-methoxyphenol, TCI) was firstly dissolved in cold ethanol (cooled in an ice bath), and
273 then mixed with equal molar amount of HI solution and stirred at 0 °C for 2 h. VBAI solids
274 were obtained by adding diethyl ether in the mixed solution, followed by filtration and wash
275 using diethyl ether. The VBAI solids was finally dried in the N₂ glove-box at 50 °C for 24 h.

276 *Perovskite film preparation and characterizations.* Quasi-2D perovskite (VBA)₂(MA)_{n-1}Pb_nI_{3n+1}
277 (or (PMA)₂(MA)_{n-1}Pb_nI_{3n+1}) solution was prepared by dissolving stoichiometric quantities of
278 PbI₂, MAI and VBAI (or PMAI) mixture in DMF with a concentration of 0.3 M, and stirred
279 for overnight before use. Quasi-2D perovskite (VBA)₂(FA_{0.83}CS_{0.17})_{n-1}Pb_n(I_{0.9}Br_{0.1})_{3n+1} (or
280 (PMA)₂(FA_{0.83}CS_{0.17})_{n-1}Pb_n(I_{0.9}Br_{0.1})_{3n+1}) solution was prepared using a similar method. The
281 perovskite solutions were spin coated on cleaned glass substrates at 5,000 r.p.m. for 60 s, and
282 toluene was dropped on the spinning substrate at around 1-2 seconds before the spinning the
283 perovskite film change color. The thickness of perovskite films, around 50 nm, was measured
284 using a Dektak XT profiler. The perovskite films were annealed at 80 °C for 10 min to remove
285 solvent residue. The polymerization process was conducted using a UV lamp (wavelength: 254
286 nm; intensity: 0.1 W/cm²).

287 XRD measurements were performed with a SmartLab diffractometer with the Bragg-
288 Brentano parallel beam geometry, and a conventional Cu target X-ray tube was set to 40 kV

289 and 150 mA. FTIR measurements were conducted using the Nicolet 8700 with a spectral range
290 from 4000 to 500 cm^{-1} , with an Attenuated Total Reflection (ATR) accessory. ^1H NMR spectra
291 were acquired at room temperature on Bruker AVANCE III NMR Spectrometers with a 400
292 MHz Bruker magnet. All chemical shifts were reported in ppm relative to tetramethylsilane
293 (TMS). Films were redissolved in d_6 -DMSO for measurements. GPC were measured with
294 Waters PL-GPC50 apparatus, and DMF were employed as an eluent at a flow rate of 1.0
295 mL/min. Films were redissolved in DMF for measurements. The SEM images were collected
296 in a GeminiSEM 500 with an accelerating voltage of 3 kV. The HRTEM images were obtained
297 using a JEM-2100F system. TGA measurements were acquired via a STA 6000 thermal
298 analysis system, heating at a rate of 10 $^\circ\text{C}/\text{min}$ from 30 to 700 $^\circ\text{C}$ under a constant 50 mL/min
299 N_2 gas flow. UPS data were obtained using a ESCALAB 250Xi spectrometer with He I
300 radiation (21.2 eV) at a pass energy (PE) of 2 eV. Absorption spectra were measured using a
301 Perkin Elmer Lambda 950 UV-vis-NIR spectrometer. The steady-state PL and PLQY data were
302 measured using a Horiba Fluorolog-3 system with Petite Integrating Sphere. The excitation
303 wavelength was 450 nm provided by a Xe lamp. The TRPL were taken using a Horiba time-
304 correlated single-photon counting system. The samples were excited by a pulsed laser diode
305 (NanoLED-Horiba) with a center wavelength of 369 nm, an excitation intensity of 0.6 mW/cm^2 ,
306 and a repetition rate that was less than the reciprocal of the measurement range. The TRPL
307 curves were fitting with 2-exponential components. The refractive index of perovskite films
308 was measured by a J. A. Woollam variable angle spectroscopic ellipsometer. All samples were
309 spin-coated on Si wafers and the spectra were fitted using the model of “Si with absorbing film.”

310 Temperature-dependent measurement of PL and TRPL were conducted using a N_2 cryostat

311 (Optistat DN-V, Oxford Instruments). Temperature was controlled by a cryogenic environment
312 controller (Mercury iTC, Oxford Instruments). All temperatures were stabilized for 15 min
313 before measurement. The PLQY values at different temperatures were calibrated using PLQY
314 values at room temperature.

315 *PeLED fabrication and characterizations.* Pre-patterned ITO substrates were sequentially
316 sonicated with deionized water, acetone, and ethanol for 20 min. The substrates were treated
317 by ultraviolet-ozone for 10 min before use. Poly-TPD solution (6 mg/mL in CB) was spin-
318 coated on the ITO substrates at 1,000 rpm for 60 s, followed by thermal annealing at 150 °C
319 for 20 min. The poly-TPD layer was treated by O₂ plasma for 5 s to improve wetting. TPBi,
320 LiF and Al layers were sequentially evaporated on top of the perovskite film with thicknesses
321 of 40, 1.2 and 100 nm, respectively. The device area was 0.04 cm².

322 The performance of PeLEDs were measured in a N₂ glove-box using a homemade
323 motorized goniometer setup consisting of a Keithley 2400 sourcemeter unit, a calibrated Si
324 photodiode (FDS-100-CAL, Thorlabs), a picoammeter (4140B, Agilent), and a calibrated fiber
325 optic spectrophotometer (UVN-SR, StellarNet Inc.). The current density-voltage (J-V) curve
326 was obtained by scanning the voltage from -0.5 to 5 V (forward scan) with a step of 0.05 V.
327 Temperature-dependent of PeLED and SCLC measurement were conducted using N₂ cryostat
328 mentioned above. Si photodiode and fiber probe were attached to the quartz window of the
329 cryostat. The EQEs values at different temperatures were calibrated using EQE value at room
330 temperature.

331 *Computational method.* Ab initio molecular dynamics (AIMD) simulations and electronic
332 structure calculations were performed using the Vienna ab initio simulation package (VASP)⁴⁰.

333 Projector-augmented wave pseudopotentials were employed to describe the electron-nuclei
334 interactions^{41,42}, and the Perdew-Burke-Ernzerhof (PBE) exchange-correlation functional were
335 used in all calculations⁴³. The Kohn-Sham wave functions were expanded in plane waves up
336 to 400 eV. We used a $3\times 3\times 1$ mesh grid to sample the K-space uniformly. The convergence
337 threshold of energy in the self-consistent step was set to 10^{-5} eV with Gaussian smearing of
338 0.01 eV/Å. Moreover, the force threshold of geometry optimization is 0.02 eV/Å for each
339 dimension of all atoms in the supercell. The elastic tensor was determined by performing six
340 finite lattice distortions, and the elastic constants were derived from the strain-stress
341 relationship⁴⁴. The effective masses of free carriers were derived by fitting E-k diagram near
342 band extremum by a parabola. Ion-clamped dielectric constants of anionic and organic layers
343 were estimated in frozen configurations using density functional perturbation theory⁴⁵. AIMD
344 were used to reveal atomic displacement at specific temperature (80, 300 and 380 K after
345 geometry optimization). Then, a 5 ps microcanonical AIMD trajectory was then generated with
346 a time step of 1 fs. Finally, the root mean squared displacement (RMSD) was evaluated by
347 comparing to optimum configuration. The phonons at Γ point were calculated by finite-
348 displacement method implemented in the PHONOPY package with step of 0.015 Å⁴⁶. Here, we
349 taken VASP as the force-constant calculator with a high plane waves cutoff at 500 eV, and the
350 force evaluations were performed on $1\times 1\times 1$ supercells using k-point sampling meshes $2\times 2\times 2$.
351 *Deformation potential calculation.* Deformation potential (D) is defined as the change in the
352 bandgap energy per unit strain due to phonon scattering, which has been used to describe the
353 electron-phonon interaction⁴⁷. To estimate D , the temperature-dependent FWHM of
354 $(\text{PVBA})_2\text{PbI}_4$ and $(\text{PMA})_2\text{PbI}_4$ were fitted by the following model⁴⁸

$$\Gamma(T) = \Gamma_0 + \gamma_{ac}T + \frac{\Gamma_{LO}}{e^{\hbar\omega_{LO}/k_B T} - 1} + \Gamma_{imp}e^{-E_{imp}/k_B T}$$

where Γ_0 is the temperature-independent inhomogeneous broadening; γ_{ac} is the acoustic phonon interaction constant; Γ_{LO} is the optical phonon interaction constant; $\hbar\omega_{LO}$ represents the optical phonon energy; Γ_{imp} is the PL broadening from the completely ionized impurity states; E_{imp} is the average energy of the impurities ionizing, and k_B and T correspond to the Boltzmann constant and the temperature, respectively.

The homopolar optical phonon scattering has been proved to be the main sources of scattering by the relaxation mechanism at high temperature¹⁴. Thus, the contribution of charge impurities and acoustic phonons to the broadening can be ignored¹⁶:

$$FWHM = \Gamma_0 + \frac{\Gamma_{homo}}{e^{\hbar\omega_{homo}/k_B T} - 1}$$

At high temperature, Γ_{homo} is approximated as:

$$\Gamma_{homo} = \frac{\hbar M \omega_{homo}}{\rho L} \left(\frac{D}{\hbar \omega_{homo}} \right)^2$$

where $M = m_e^* + m_h^*$ is the sum of electron and hole effective masses (Supplementary Table 2); ω_{homo} is the homopolar phonon angular frequency; ρ is the mass density (2.7 g/cm³ for both materials)¹⁶; L is the thickness of quantum well where the excitation is confined ($L = 0.64$ nm for Pb-I-Pb inorganic layer).

Trap density and carrier mobility calculation. The trap density and carrier mobility were calculated using SCLC results. The hole-only device structure is ITO/poly-TPD (40 nm)/2D perovskite (100 nm)/poly-TPD (40 nm)/MoO₃ (10 nm)/Ag (100 nm) (ITO: indium tin oxide, poly-TPD: poly[N,N'-bis (4-butylphenyl)-N,N'-bis(phenyl)-benzidine]). The electron-only device structure is ITO/SnO₂ (20 nm)/2D perovskite (100 nm)/TPBi (40 nm)/LiF (1.2 nm)/Al (100 nm) (TPBi: 2,2',2''-(1,3,5-Benzinetriyl)-tris(1-phenyl-1-H-benzimidazole)). Three

377 distinct regions could be identified from the I - V curves including Ohmic, trap-filled limited
378 (TFL) as well as SCLC regions. The hole and electron trap density were extract from hole and
379 electron only devices, respectively, using equation⁴⁹

$$380 \quad N_{traps} = 2\varepsilon_0\varepsilon_r V_{TFL}/(qL^2)$$

381 where the ε_0 , ε_r , V_{TFL} , q and L are the vacuum permittivity, the relative dielectric constant, the
382 onset voltage of the TFL region, elementary charge and the thickness of the perovskite films,
383 respectively.

384 The charge carrier mobility was extracted from the SCLC regions using the Mott-Gurney
385 Law⁴⁹:

$$386 \quad J = \frac{9\varepsilon_0\varepsilon_r\mu V^2}{8L^3}$$

387 where μ is the charge mobility, J and V are current density and applied voltage, respectively.

388 *Optical modelling.* The light outcoupling calculations were based on a classical dipole emission
389 model⁵⁰. The power ratio radiated to each in-plane wavevector range (outcoupled, substrate,
390 waveguided, surface plasmon polariton) was simulated by using the experimentally obtained
391 optical constants (refractive index) of each layer to construct the model device. The refractive
392 indexes of perovskite were obtained by ellipsometry. The dipole position was assumed to be at
393 the center of perovskite layer.

394 **Data availability**

395 The data that support the findings of this study are available from the corresponding author
396 upon reasonable request.

397 **References**

398 1. Liu, X. K. *et al.* Metal halide perovskites for light-emitting diodes. *Nat. Mater.* **20**, 10-21

- 399 (2021).
- 400 2. Kim, G. *et al.* Impact of strain relaxation on performance of alpha-formamidinium lead
401 iodide perovskite solar cells. *Science* **370**, 108-112 (2020).
- 402 3. Wei, H. & Huang, J. Halide lead perovskites for ionizing radiation detection. *Nat. Commun.*
403 **10**, 1066 (2019).
- 404 4. Nayak, P. K., Mahesh, S., Snaith, H. J. & Cahen, D. Photovoltaic solar cell technologies:
405 analysing the state of the art. *Nat. Rev. Mater.* **4**, 269-285 (2019).
- 406 5. Thouin, F. *et al.* Phonon coherences reveal the polaronic character of excitons in two-
407 dimensional lead halide perovskites. *Nat. Mater.* **18**, 349-356 (2019).
- 408 6. Chu, W., Zheng, Q., Prezhdo, O. V., Zhao, J. & Saidi, W. A. Low-frequency lattice phonons
409 in halide perovskites explain high defect tolerance toward electron-hole recombination.
410 *Sci. Adv.* **6**, eaaw7453 (2020).
- 411 7. Shi, E. *et al.* Two-dimensional halide perovskite lateral epitaxial heterostructures. *Nature*
412 **580**, 614-620 (2020).
- 413 8. Akkerman, Q. A., Raino, G., Kovalenko, M. V. & Manna, L. Genesis, challenges and
414 opportunities for colloidal lead halide perovskite nanocrystals. *Nat. Mater.* **17**, 394-405
415 (2018).
- 416 9. Wang, Y. *et al.* Stabilizing heterostructures of soft perovskite semiconductors. *Science* **365**,
417 687-691 (2019).
- 418 10. Wright, A. D. *et al.* Electron-phonon coupling in hybrid lead halide perovskites. *Nat.*
419 *Commun.* **7**, 11755 (2016).
- 420 11. Cho, H. *et al.* High-Efficiency Solution-Processed Inorganic Metal Halide Perovskite

- 421 Light-Emitting Diodes. *Adv. Mater.* **29**, 1700579 (2017).
- 422 12. Ren, H. *et al.* Efficient and stable Ruddlesden–Popper perovskite solar cell with tailored
423 interlayer molecular interaction. *Nat. Photonics* **14**, 154-163 (2020).
- 424 13. Chen, Z., Guo, Y., Wertz, E. & Shi, J. Merits and Challenges of Ruddlesden–Popper Soft
425 Halide Perovskites in Electro-Optics and Optoelectronics. *Adv. Mater.* **31**, 1803514 (2019).
- 426 14. Gong, X. *et al.* Electron-phonon interaction in efficient perovskite blue emitters. *Nat.*
427 *Mater.* **17**, 550-556 (2018).
- 428 15. Zhang, L. *et al.* Bright Free Exciton Electroluminescence from Mn-Doped Two-
429 Dimensional Layered Perovskites. *J. Phys. Chem. Lett.* **10**, 3171-3175 (2019).
- 430 16. Guo, Z., Wu, X., Zhu, T., Zhu, X. & Huang, L. Electron-Phonon Scattering in Atomically
431 Thin 2D Perovskites. *ACS Nano* **10**, 9992-9998 (2016).
- 432 17. Era, M., Morimoto, S., Tsutsui, T. & Saito, S. Organic - inorganic heterostructure
433 electroluminescent device using a layered perovskite semiconductor $(\text{C}_6\text{H}_5\text{C}_2\text{H}_4\text{NH}_3)_2\text{PbI}_4$.
434 *Appl. Phys. Lett.* **65**, 676-678 (1994).
- 435 18. Li, X. *et al.* In-situ cross-linking strategy for efficient and operationally stable
436 methylammonium lead iodide solar cells. *Nat. Commun.* **9**, 3806 (2018).
- 437 19. Wang, R. *et al.* Constructive molecular configurations for surface-defect passivation of
438 perovskite photovoltaics. *Science* **366**, 1509-1513 (2019).
- 439 20. Na Quan, L. *et al.* Edge stabilization in reduced-dimensional perovskites. *Nat. Commun.*
440 **11**, 170 (2020).
- 441 21. Zhao, Y. *et al.* A Polymerization-Assisted Grain Growth Strategy for Efficient and Stable
442 Perovskite Solar Cells. *Adv. Mater.* **32**, e1907769 (2020).

- 443 22. Guo, P. *et al.* Double Barriers for Moisture Degradation: Assembly of Hydrolysable
444 Hydrophobic Molecules for Stable Perovskite Solar Cells with High Open-Circuit Voltage.
445 *Adv. Funct. Mater.* **30**, 2002639 (2020).
- 446 23. Bi, D. *et al.* Polymer-templated nucleation and crystal growth of perovskite films for solar
447 cells with efficiency greater than 21%. *Nat. Energy* **1**, 16142 (2016).
- 448 24. Tieke, B. & Chapuis, G. Solid State Polymerization of Butadienes in Layer Structures. *Mol.*
449 *Cryst. Liq. Cryst.* **137**, 101-116 (1986).
- 450 25. Kosuge, H., Okada, S., Oikawa, H. & Nakanishi, H. Polydiacetylenes in Organic-Inorganic
451 Hybrid Systems. *Mol. Cryst. Liq. Cryst.* **377**, 13-18 (2002).
- 452 26. Proppe, A. H. *et al.* Photochemically Cross-Linked Quantum Well Ligands for 2D/3D
453 Perovskite Photovoltaics with Improved Photovoltage and Stability. *J. Am. Chem. Soc.* **141**,
454 14180-14189 (2019).
- 455 27. Deng, J.-P., Yang, W.-T. & Rånby, B. Auto-Initiating Performance of Styrene on Surface
456 Photografting Polymerization. *Macromol. Rapid Commun.* **22**, 535-538 (2001).
- 457 28. Tremblay, M.-H. *et al.* Structures of $(4\text{-Y-C}_6\text{H}_4\text{CH}_2\text{NH}_3)_2\text{PbI}_4$ {Y = H, F, Cl, Br, I}: Tuning
458 of Hybrid Organic Inorganic Perovskite Structures from Ruddlesden–Popper to Dion–
459 Jacobson Limits. *Chem. Mater.* **31**, 6145-6153 (2019).
- 460 29. Mehdizadeh, A., Akhtarianfar, S. F. & Shojaei, S. Role of Methylammonium Rotation in
461 Hybrid Halide MAPbX_3 (X = I, Br, and Cl) Perovskites by a Density Functional Theory
462 Approach: Optical and Electronic Properties. *J. Phys. Chem. C* **123**, 6725-6734 (2019).
- 463 30. Gonzalez-Carrero, S., Espallargas, G. M., Galian, R. E. & Pérez-Prieto, J. Blue-
464 luminescent organic lead bromide perovskites: highly dispersible and photostable

- 465 materials. *J. Mater. Chem. A* **3**, 14039-14045 (2015).
- 466 31. Ni, L. *et al.* Real-Time Observation of Exciton-Phonon Coupling Dynamics in Self-
467 Assembled Hybrid Perovskite Quantum Wells. *ACS Nano* **11**, 10834-10843 (2017).
- 468 32. Chu, W., Saidi, W. A., Zhao, J. & Prezhdo, O. V. Soft Lattice and Defect Covalency
469 Rationalize Tolerance of β -CsPbI₃ Perovskite Solar Cells to Native Defects. *Angew.*
470 *Chem. Int. Ed.* **59**, 6435-6441 (2020).
- 471 33. Herz, L. M. Charge-Carrier Mobilities in Metal Halide Perovskites: Fundamental
472 Mechanisms and Limits. *ACS Energy Lett.* **2**, 1539-1548 (2017).
- 473 34. Karakus, M. *et al.* Phonon-Electron Scattering Limits Free Charge Mobility in
474 Methylammonium Lead Iodide Perovskites. *J. Phys. Chem. Lett.* **6**, 4991-4996 (2015).
- 475 35. Shrestha, S. *et al.* Assessing Temperature Dependence of Drift Mobility in
476 Methylammonium Lead Iodide Perovskite Single Crystals. *J. Phys. Chem. C* **122**, 5935-
477 5939 (2018).
- 478 36. Yuan, M. *et al.* Perovskite energy funnels for efficient light-emitting diodes. *Nat. Nanotech.*
479 **11**, 872-877 (2016).
- 480 37. Wang, N. *et al.* Perovskite light-emitting diodes based on solution-processed self-
481 organized multiple quantum wells. *Nat. Photonics* **10**, 699-704 (2016).
- 482 38. Rehman, W. *et al.* Photovoltaic mixed-cation lead mixed-halide perovskites: links between
483 crystallinity, photo-stability and electronic properties. *Energy Environ. Sci.* **10**, 361-369
484 (2017).
- 485 39. Richter, J. M. *et al.* Enhancing photoluminescence yields in lead halide perovskites by
486 photon recycling and light out-coupling. *Nat. Commun.* **7**, 13941 (2016).

- 487 40. Kresse, G. & Hafner, J. Ab initio molecular dynamics for open-shell transition metals.
488 *Phys. Rev. B* **48**, 13115-13118 (1993).
- 489 41. Blochl, P. E. Projector augmented-wave method. *Phys. Rev. B* **50**, 17953-17979 (1994).
- 490 42. Kresse, G. & Joubert, D. From ultrasoft pseudopotentials to the projector augmented-wave
491 method. *Phys. Rev. B* **59**, 1758-1775 (1999).
- 492 43. Perdew, J. P., Burke, K. & Ernzerhof, M. Generalized Gradient Approximation Made
493 Simple. *Phys. Rev. Lett.* **77**, 3865-3868 (1996).
- 494 44. Le Page, Y. & Saxe, P. Symmetry-general least-squares extraction of elastic data for
495 strained materials from ab initio calculations of stress. *Phys. Rev. B* **65**, 104104 (2002).
- 496 45. Gajdoš, M., Hummer, K., Kresse, G., Furthmüller, J. & Bechstedt, F. Linear optical
497 properties in the projector-augmented wave methodology. *Phys. Rev. B* **73**, 045112 (2006).
- 498 46. Chaput, L., Togo, A., Tanaka, I. & Hug, G. Phonon-phonon interactions in transition
499 metals. *Phys. Rev. B* **84**, 094302 (2011).
- 500 47. Franceschetti, A., Wei, S. H. & Zunger, A. Absolute deformation potentials of Al, Si, and
501 NaCl. *Phys. Rev. B* **50**, 17797-17801 (1994).
- 502 48. Handa, T., Aharen, T., Wakamiya, A. & Kanemitsu, Y. Radiative recombination and
503 electron-phonon coupling in lead-free CH₃NH₃SnI₃ perovskite thin films. *Phys. Rev. Mater.*
504 **2**, 075402 (2018).
- 505 49. Dong, Q. *et al.* Electron-hole diffusion lengths > 175 μm in solution-grown CH₃NH₃PbI₃
506 single crystals. *Science* **347**, 967-970 (2015).
- 507 50. Furno, M., Meerheim, R., Hofmann, S., Lüssem, B. & Leo, K. Efficiency and rate of
508 spontaneous emission in organic electroluminescent devices. *Phys. Rev. B* **85**, 115205

509 (2012).

510 **Acknowledgements**

511 We acknowledge the support from the National Natural Science Foundation of China (NSFC,
512 Award # 51872274) and the Fundamental Research Funds for the Central Universities
513 (WK2060190053). This work was partially carried out at the University of Science and
514 Technology of China Center for Micro and Nanoscale Research and Fabrication.

515 **Author contributions**

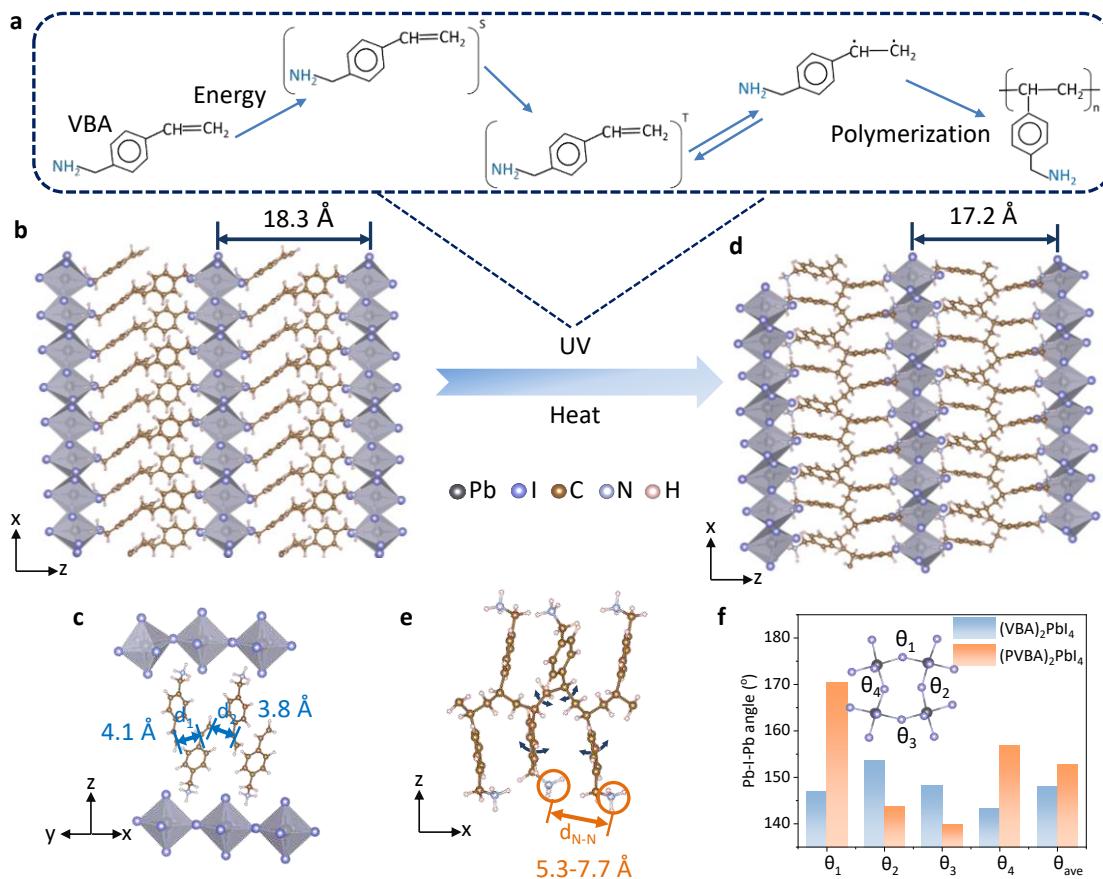
516 Z.X. conceived the idea and supervised the project. W.C. fabricated and characterized the
517 perovskite films and PeLEDs. Y.S., Y.L. and J.Z. did the theoretical simulation. J.C. carried out
518 the temperature-dependent SCLC measurement. P.M. did the optical simulations of the
519 PeLEDs. Z.F. conducted the absorption and PL characterizations. Y.D. and W.C. synthesized
520 VBAI. Z.X. and W.C. wrote the manuscript, and all authors reviewed the manuscript.

521 **Competing financial interests**

522 The authors declare no competing financial interests.

523 .

524



525

526 **Fig. 1 | Theoretical calculation of polymerized perovskite structure. a,** The polymerization

527 process of VBA monomers. **b,c,** Molecular structure of (VBA)₂PbI₄ perovskite (**b**) and the

528 VBA monomer configuration in the perovskite lattice (**c**). d_1 and d_2 represent the distance

529 between two adjacent C=C functional groups in the perovskite lattice. **d,e,** Molecular structure

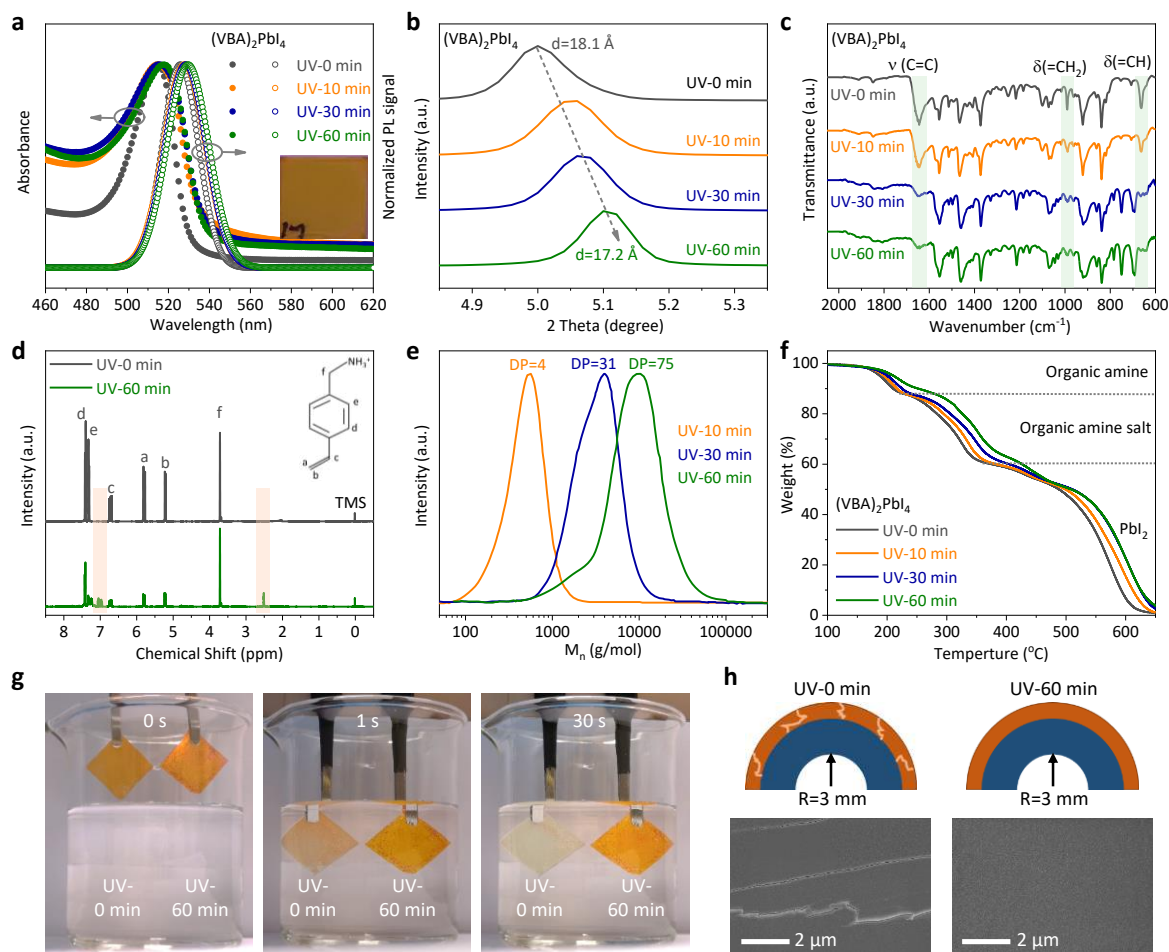
530 of (PVBA)₂PbI₄ perovskite (**d**) and PVBA polymer configuration (**e**). The bending arrows

531 represent the rotation direction of carbon-carbon bond. **f,** Pb-I-Pb bond angles for (VBA)₂PbI₄

532 and (PVBA)₂PbI₄.

533

534



535

536 **Fig. 2 | Experimental demonstration of the formation of polymerized perovskite and its**

537 **polymer-like behavior. a-f**, Absorption and PL spectra (a), XRD patterns (b), FTIR spectra

538 (c), ¹H NMR spectra (d), GPC traces (e) and TGA curves (f) for (VBA)₂PbI₄ films with various

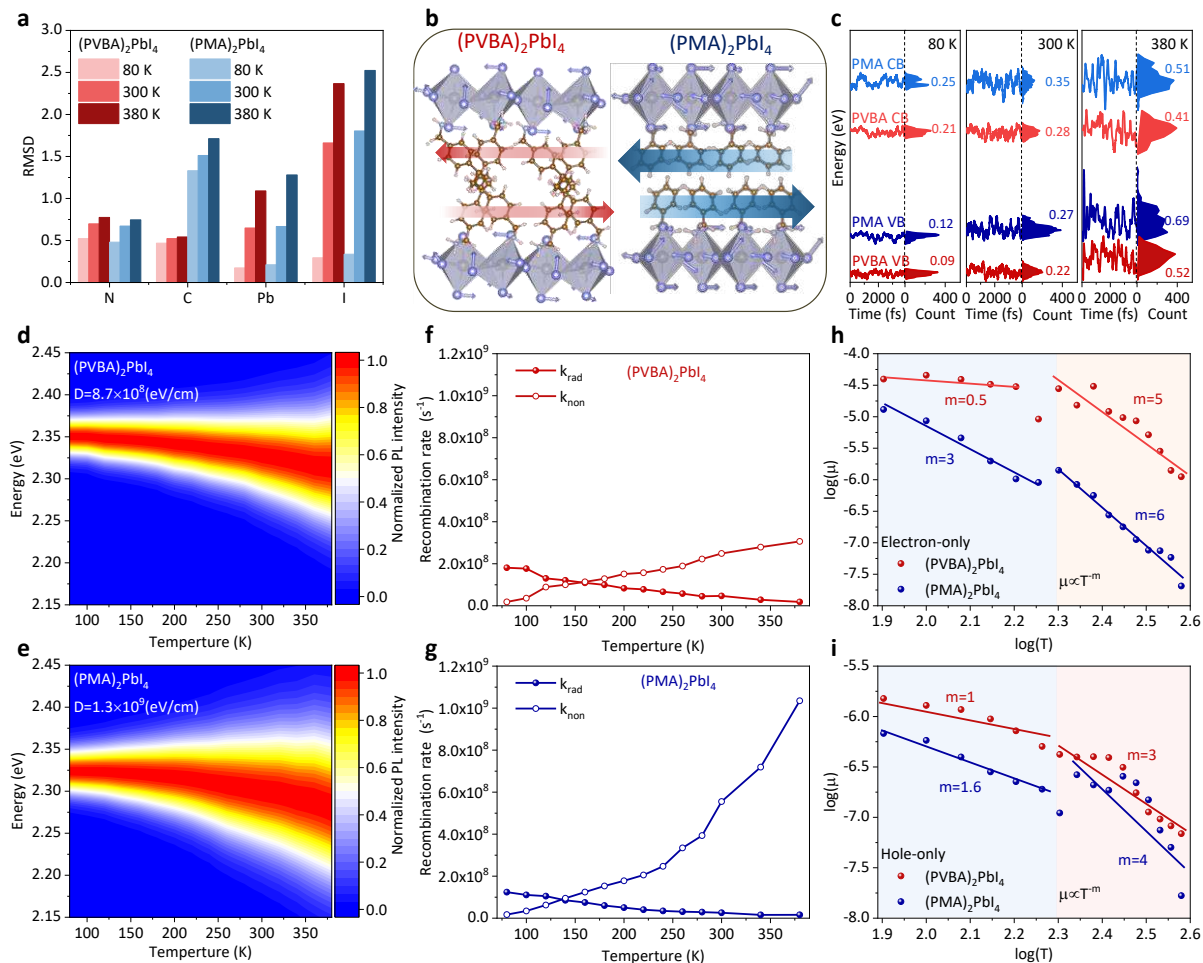
539 UV exposure durations. Inset in (a): A photograph of an as-prepared (VBA)₂PbI₄ film. **g**,

540 Photographs of the (VBA)₂PbI₄ and (PVBA)₂PbI₄ perovskite films immersed in water for

541 different durations. **h**, Schematic illustrations and corresponding SEM images of the

542 (VBA)₂PbI₄ and (PVBA)₂PbI₄ perovskite films (thickness: 500 nm) after 500 bending cycles

543 with a bending radius of 3 mm.



544

545 **Fig. 3 | Enhanced rigidity of the polymerized perovskite and its influence on**

546 **optoelectronic properties. a**, Average atomic displacement of N, C, Pb and I atoms of

547 $(PVBA)_2PbI_4$ and $(PMA)_2PbI_4$ from DFT calculation. **b**, Real-space displacement of the

548 dominated modes of $(PVBA)_2PbI_4$ and $(PMA)_2PbI_4$ structures. The arrow direction and

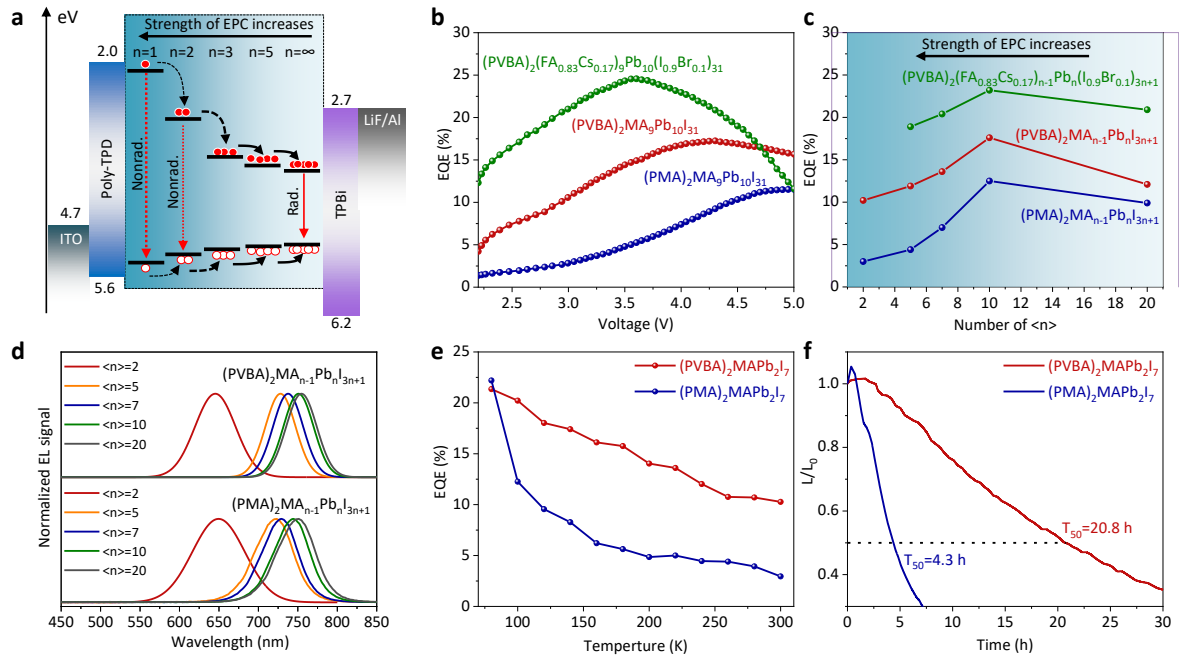
549 thickness represent direction and intensity of atom vibration, respectively. **c**, Bandedge

550 fluctuations and corresponding histograms for $(PVBA)_2PbI_4$ and $(PMA)_2PbI_4$. The numbers are

551 the FWHM values of the histograms. **d-i**, Temperature-dependent steady-state PL spectra (**d,e**),

552 k_{rad} and k_{non} (**f,g**), and electron/hole mobilities (**h,i**) of both $(PVBA)_2PbI_4$ and $(PMA)_2PbI_4$.

553



554

555 **Fig. 4 | Device performances of polymerized PeLEDs. a,** Energy diagram of quasi-2D

556 PeLEDs. Rad. and Nonrad. represent radiative recombination and non-radiative recombination,

557 respectively. **b,** EQE curves of the PeLEDs based on different quasi-2D perovskites. **c,d,** EQE

558 values (**c**) and EL spectra (**d**) of the quasi-2D PeLEDs with different $\langle n \rangle$ values. **e,**

559 Temperature-dependent peak EQE of $(PVBA)_2MAPb_2I_7$ and $(PMA)_2MAPb_2I_7$ based PeLEDs.

560 **f,** Operation stability of the PeLEDs measured at a constant current density of 5 mA/cm^2 .

561

Figures

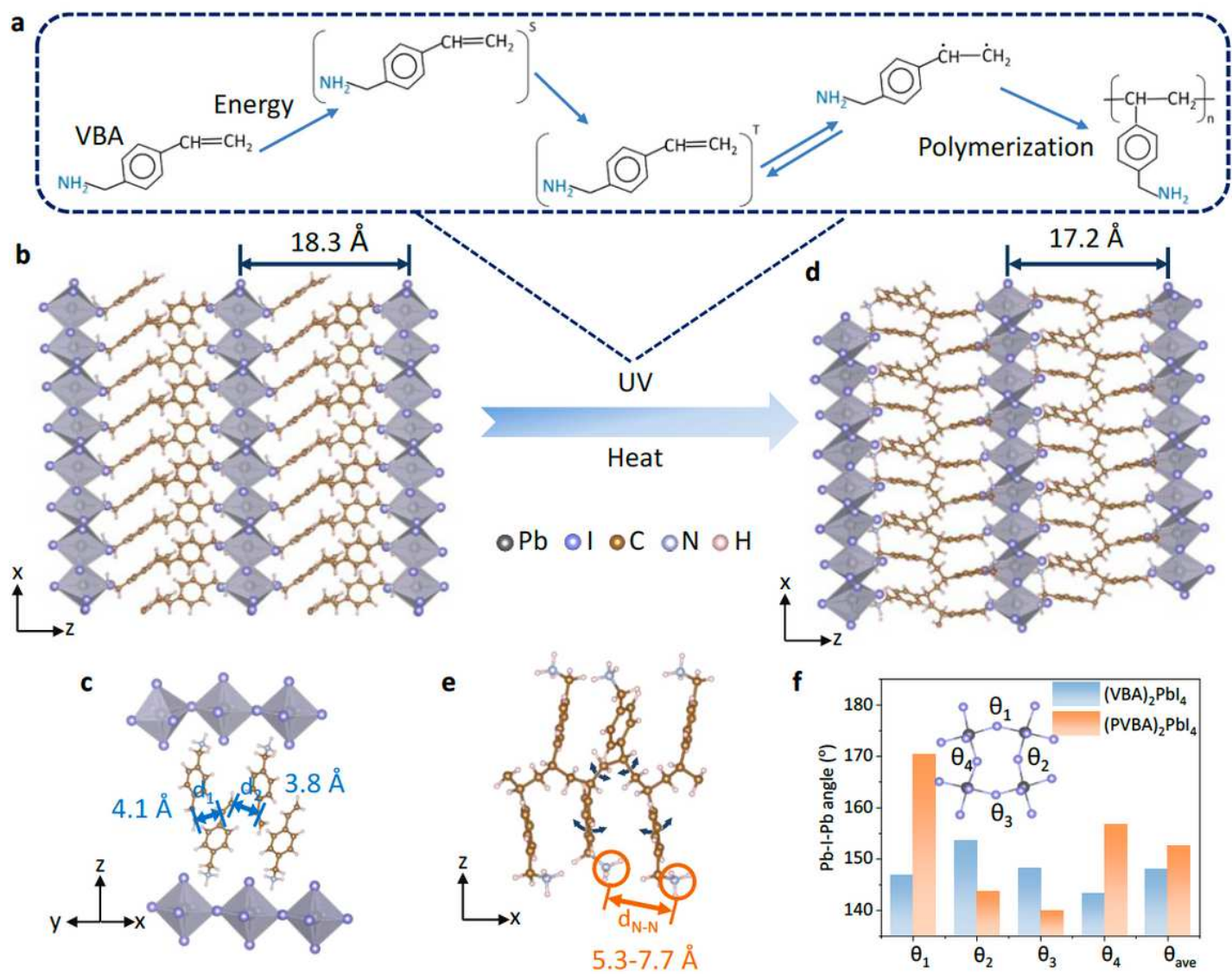


Figure 1

Theoretical calculation of polymerized perovskite structure.

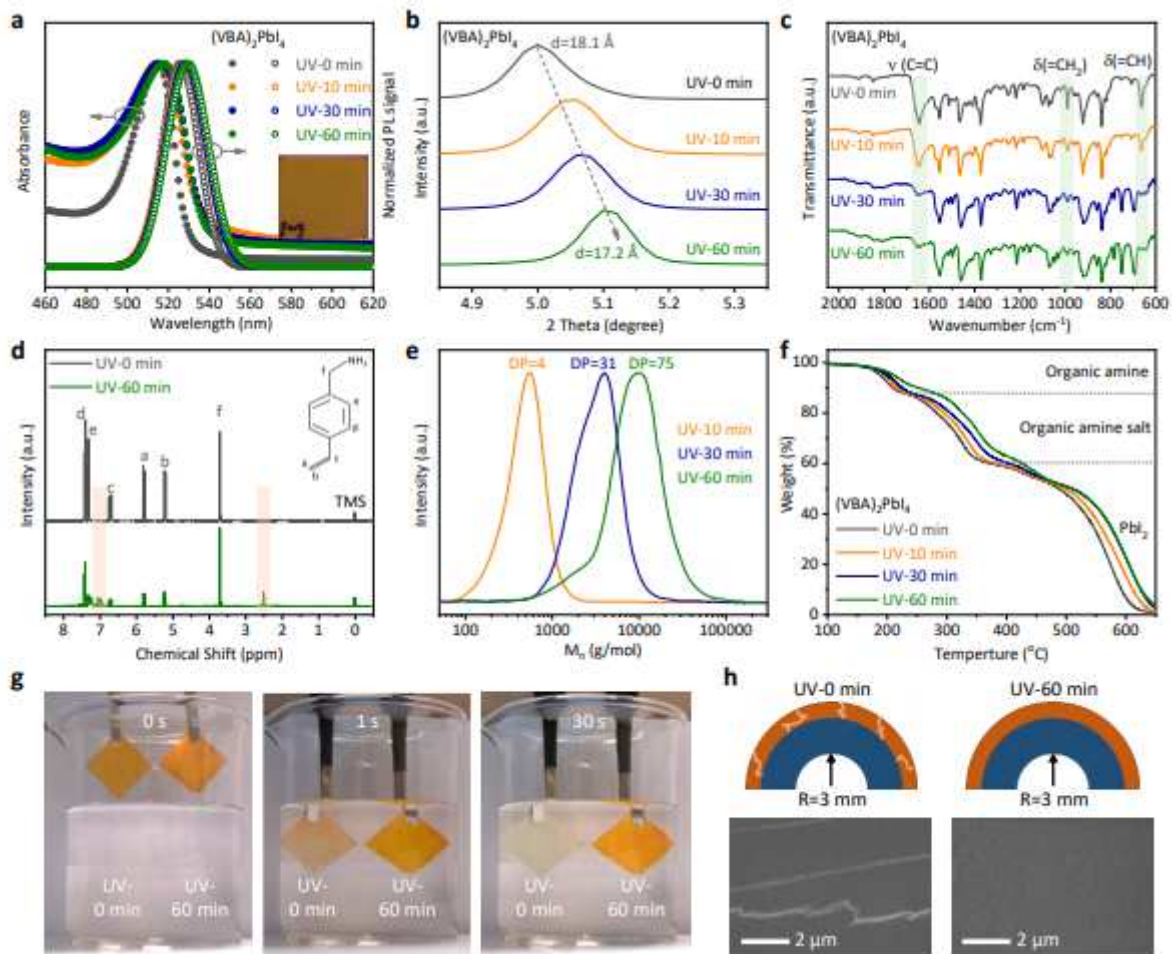


Figure 2

Experimental demonstration of the formation of polymerized perovskite and its polymer-like behavior.

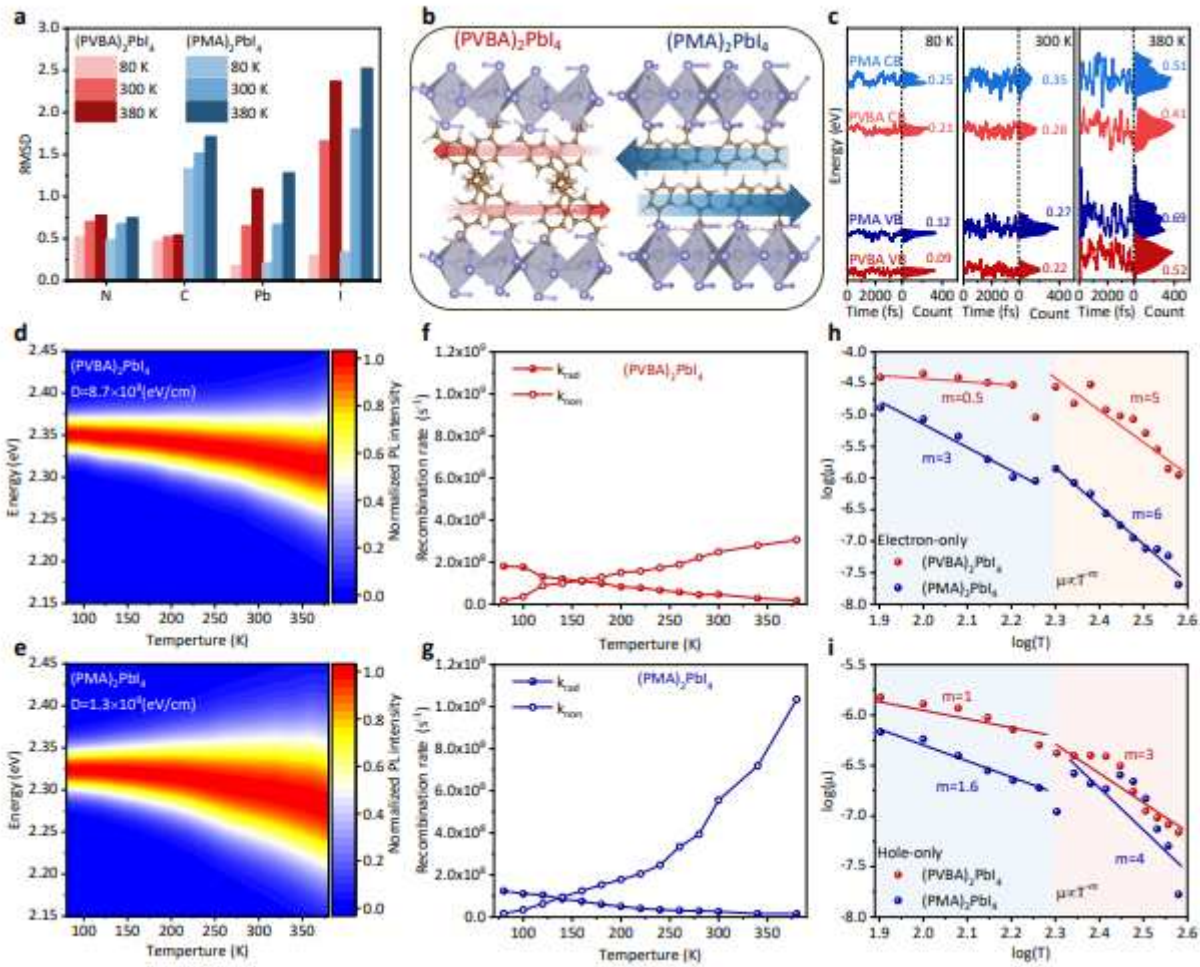


Figure 3

Enhanced rigidity of the polymerized perovskite and its influence on optoelectronic properties.

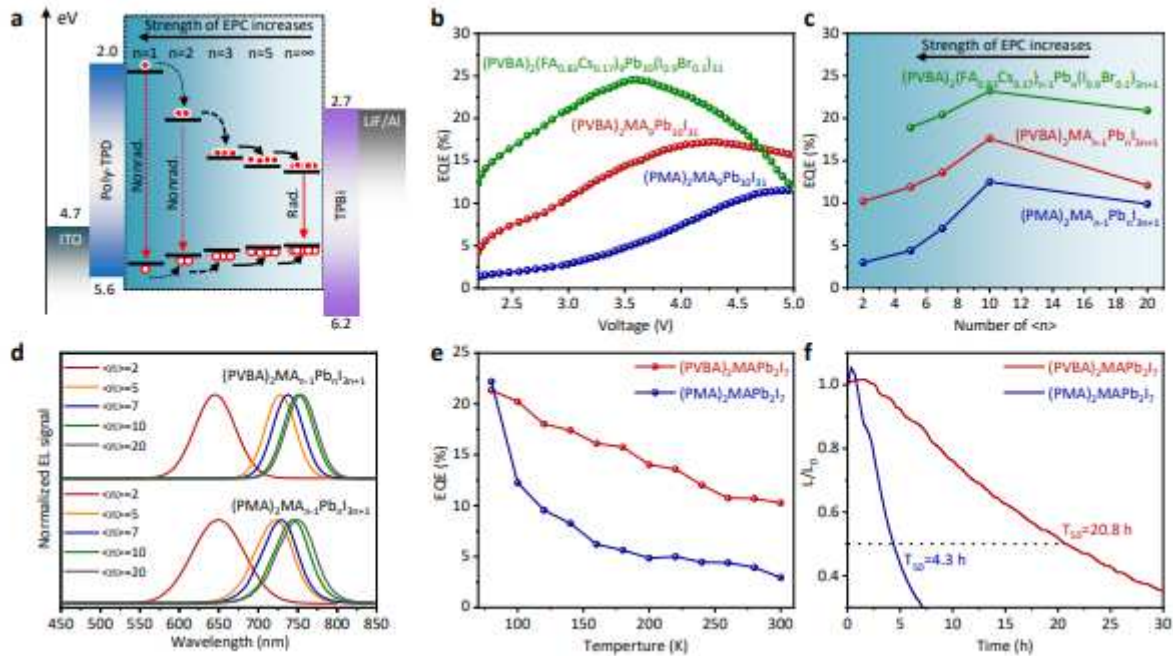


Figure 4

Device performances of polymerized PeLEDs.

Supplementary Files

This is a list of supplementary files associated with this preprint. Click to download.

- [SupplementaryVideo.mov](#)
- [RevisedSupplementaryInformation.pdf](#)